Review of Scientific Instruments

A highly automated apparatus for ultra-fast laser ablation studies

Cite as: Rev. Sci. Instrum. **93**, 073003 (2022); https://doi.org/10.1063/5.0095719
Submitted: 12 April 2022 • Accepted: 23 June 2022 • Published Online: 18 July 2022

Marnix Vreugdenhil and Dries van Oosten

View Online Export Citation CrossMark

ARTICLES YOU MAY BE INTERESTED IN

A novel design for the combination of electrochemical atomic force microscopy and Raman spectroscopy in reflection mode for in situ study of battery materials
Review of Scientific Instruments **93**, 073707 (2022); https://doi.org/10.1063/5.0096766

Time-of-flight mass spectrometer for diagnostics of continuous plasma flow
Review of Scientific Instruments **93**, 073505 (2022); https://doi.org/10.1063/5.0096621

Spectroscopic depth profilometry of organic thin films upon inductively coupled plasma etching
Review of Scientific Instruments **93**, 073903 (2022); https://doi.org/10.1063/5.0088718

Lock-in Amplifiers up to 600 MHz
Zurich Instruments
Watch

© 2022 Author(s).

Review of Scientific Instruments ARTICLE scitation.org/journal/rsi

A highly automated apparatus for ultra-fast laser ablation studies

Cite as: Rev. Sci. Instrum. 93, 073003 (2022); doi: 10.1063/5.0095719
Submitted: 12 April 2022 • Accepted: 23 June 2022 •
Published Online: 18 July 2022

View Online Export Citation CrossMark

Marnix Vreugdenhil[a] and Dries van Oosten[b]

AFFILIATIONS

Debye Institute for Nanomaterials Science and Center for Extreme Matter and Emergent Phenomena, Utrecht University, Princetonplein 5, 3584 CC Utrecht, The Netherlands

[a]Author to whom correspondence should be addressed: m.c.w.vreugdenhil@uu.nl
[b]Electronic mail: D.vanOosten@uu.nl

ABSTRACT

We present a novel experimental apparatus that can be used for extensive systematic studies of (single- and multi-shot) ultra-short laser pulse ablation. It is fully automated and generates a large number of ablation sites in a short time on a small sample surface area. For each site, the apparatus takes four *in situ* images: an image of the incident ablation beam (to determine pulse energy), a white light reference image of the pristine sample site, an image of the reflected ablation spot, and a white light image of the ablated sample site. The setup can perform ablation experiments as a function of many parameters, including pulse energy, pulse duration, number of pulses, time between pulses, and focus size. As a proof of concept, we present example results on single-shot ablation off crystalline silicon. Using only data acquired *in situ* in the presented setup, we determine the single-shot ablation threshold as a function of pulse duration and verify the threshold value using optical interferometric profilometry. The values we found agree well with literature values.

© 2022 Author(s). All article content, except where otherwise noted, is licensed under a Creative Commons Attribution (CC BY) license (http://creativecommons.org/licenses/by/4.0/). https://doi.org/10.1063/5.0095719

I. INTRODUCTION

Femtosecond laser processing of materials is a powerful tool that attracts great interest in both science[1–5] and industry. As the interaction time between the laser pulse and the material is extremely short, femtosecond laser ablation is deterministic and highly reproducible.[6–8] However, quantitatively predicting the modification threshold for a material under given illumination conditions is currently not possible. Therefore, finding the illumination parameters under which optimal modification results can be achieved is currently mostly a matter of time-consuming experimental trial and error. A predictive model of laser modification is highly sought after,[9] but lacking such a model, finding the optical illumination parameters to achieve the desired modification result requires an experimental apparatus that allows for the rapid and systematic study of laser modification in large parameter space.[10–12] This parameter space obviously includes the fluence to which the sample is exposed, but also the pulse duration,[13–17] the number of pulses,[16,18,19] the pulse repetition frequency,[18,19] laser wavelength,[20–22] and even polarization.[23]

In this work, we present a fully automated apparatus that systematically produces a matrix of many ablation sites on a small surface area. At each ablation site, the apparatus takes several *in situ* images. The apparatus is designed to work well in conjunction with an optical interferometric profilometer, to do a fast depth analysis of the ablation sites after the experiment is carried out.

An important feature of the apparatus that we present in this work is the high rate at which it can perform (single-shot) ablation experiments. This high ablation and measurement rate enables ablation experiments with a large resolution and statistical significance for a parameter in a short time. For instance, in a single typical experiment, the apparatus generates 4096 ablation sites and does four separate measurements per site. Such an experiment typically takes 3 h to complete, during which no intervention is required from the researcher. The large amount of data that the experiment produces is saved automatically in a systematic manner.

To get a better understanding of laser ablation, it is desirable to be able to do single-shot and multi-shot experiments. The combination of doing single-shot experiments and several *in situ* measurements at each site brings with it some synchronization

© Author(s) 2022

challenges. We present a detailed discussion of how the apparatus deals with these challenges.

We start by explaining the design of the apparatus and the structure of our experiments. We provide a description of how we process each type of measurement and how we structure our data analysis. To demonstrate the capabilities of the apparatus and to illustrate our analysis workflow, we present the results of a single-shot ultra-short pulse ablation experiment we carried out on crystalline silicon. Finally, we determine the single-shot laser ablation threshold as a function of pulse duration, by using only data acquired *in situ* in the presented apparatus, and find excellent agreement with literature values. All the data and analysis scripts used in this work are available as a data publication released under a Creative Commons 4.0 license.

II. THE OPTICAL PATH

Figure 1 shows a schematic overview of our main setup. The light source that we use for ablation experiments is a *Light Conversion Pharos PH2-SP-1 mJ*. This laser produces pulses at a center wavelength of 1034 nm and a full width at half maximum bandwidth of 12 nm, with a pulse repetition frequency between single-shot and 200 kHz and a maximum pulse energy of 1 mJ (at a repetition frequency of 6 kHz or lower). The grating compressor in the laser has been optimized to allow a pulse duration tunable from 170 fs up to more than 20 ps. The light from the laser is first guided through a $\lambda/2$ plate on a motorized rotation stage, followed by a polarizing beam splitter, to allow automatic scanning of the pulse energy during experiments. The pulse energy is further reduced by a neutral density filter (ND) chosen to yield a pulse energy range suitable for the sample under study. After this, the optical path contains a zoom telescope (consisting of two convex lenses and a concave lens) and

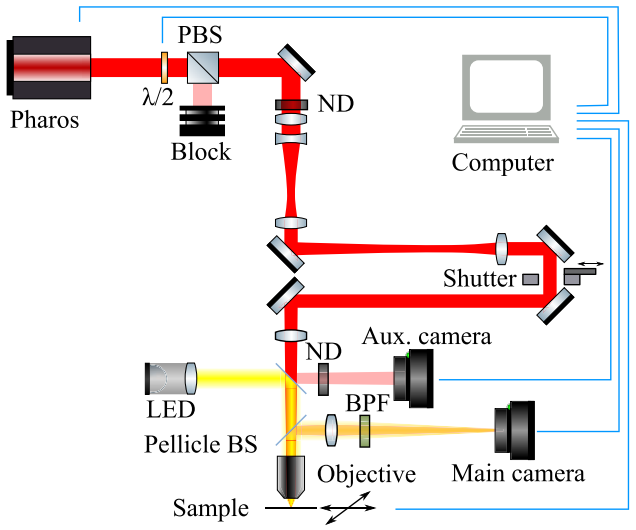

FIG. 1. A schematic of the experimental setup. $\lambda/2$: half-wave plate; PBS: polarizing beam splitter; ND: neutral density filters; Pellicle BS: pellicle beam splitters; and BPF: bandpass filter.

TABLE I. The main opto-mechanical components used in the setup.

Label	Experimental setup
Aux. camera	daA1600-60um
Main camera	Andor iXon3 885
xy translation stage	Physik Instrumente M686 PILine
z stage	Zaber T-LSM025A
$\lambda/2$ rotation	Thorlabs ELL14K
Objective	Nikon CFI60 100x

two further convex lenses. The lenses in the zoom telescope can be moved such that the beam waist can be continuously altered between ~0.7 and 5 μm. The additional lenses are used to match the output of the zoom telescope to the aperture of the objective lens. Two pellicle beam splitters (Thorlabs BP145B2 with transmission and reflection coefficients of 0.83 and 0.17, respectively, at 1034 nm) are placed in the optical path at +45° and −45° with respect to the laser propagation direction, respectively. A small part of the light is reflected by the first of these onto an auxiliary camera, which is used to determine the pulse energy (see the Appendix). A neutral density filter can be placed in front of the auxiliary camera to prevent saturation. Part of the light is transmitted by both pellicles and is focused onto the sample by using a microscope objective. The microscope objective is mounted on a linear motorized stage to enable focusing. The sample is mounted on a motorized *xy*-stage. Light reflected by the sample is collected by the microscope objective. This reflected light is then reflected by the second pellicle beam splitter and focused onto the main camera using a lens. This allows us to image the reflected ablation spot. A bandpass filter (BPF, Thorlabs FGS580) is used to attenuate the reflected ablation light to prevent saturation. Furthermore, we use a white LED to illuminate the sample in order to be able to take images of each ablation site before and after laser exposure. The white light is coupled into the optical path by overlapping it with the laser by using one of the pellicles. A lens is used to focus the white light into the back focal plane of the microscope objective to ensure wide-field illumination. White light that is reflected by the sample follows the same path as the reflected ablation light onto the main camera. The main components mentioned above are summarized in Table I.

III. DATA ACQUISITION AND SYNCHRONIZATION

We organize our experiments in runs, each consisting of several illuminations. We refer to the illumination at a single site on the sample as a shot. We refer to parameters that we vary *in between* runs as *slow parameters* and parameters that we vary *within* a run as *fast parameters*. Typically, the pulse energy will be a fast parameter, meaning that it will be changed for every shot within a run. Slow parameters might be the pulse duration, the laser wavelength, the number of pulses per shot, etc.

For every shot, we take a white light image of the pristine sample directly *before* the laser shot. Then, we take an image of ablation light reflected by the sample, which we refer to as the *during* image. Simultaneously, we take an image of the incident pulse by using the auxiliary camera. Subsequently, we take a white light image

© Author(s) 2022

of the illuminated position of the sample to record the aftermath, which we refer to as the *after* image.

To ensure synchronization between the laser and the cameras, we use the timing as illustrated in Fig. 2, in which time is given in unit of $1/R_{rep}$, where R_{rep} is the pulse repetition frequency of the regenerative amplifier (RA).

Before the ablation shot, the main camera image is acquired without triggering the laser. While taking this *before* image, the beam shutter is kept closed. The timing of the ablation shot is triggered by the acquisition of the *during* image on the main camera. A digital output from the camera (the *exp. main* signal) indicates that the camera is exposed. This signal is used to arm a single pulse generator (implemented by using the counter of a National Instruments USB-6211 card). This single pulse generator is then ready to receive a trigger. As a trigger, we use a signal from the laser that indicates when the regenerative amplifier (RA) in the laser fires (the *RA sync* signal). The pulse generator then gives a pulse that will signal the laser to open the pulse picker in time to capture the *next* RA pulse. The *exp. main* signal is also used to trigger the auxiliary camera, to ensure that it captures the same RA pulse. After the ablation shot, another main camera image is acquired of the same sample location, again without triggering the laser and with the beam shutter closed. This is the *after* image.

We control all hardware by using a graphical user interface written in Python and based on the QuDi framework.[24] With this configuration, each ablation shot takes 3 s, which is mainly limited by the acquisition, transfer, and saving of the main camera images. The experiment described in this work took 3 h, during which the apparatus ran completely automatically. We expect that the acquisition rate can be significantly improved; the technical limit of the current hardware is around 10 shots/s.

After all runs are finished, the sample is removed from the setup and placed in a Filmetrics Profilm3D optical profilometer with a 50× Nikon objective and a 4× digital zoom. The sample holder is designed to be placed reproducibly in both the ablation setup and the profilometer. Using the profilometer, we acquire height maps for all ablation sites.

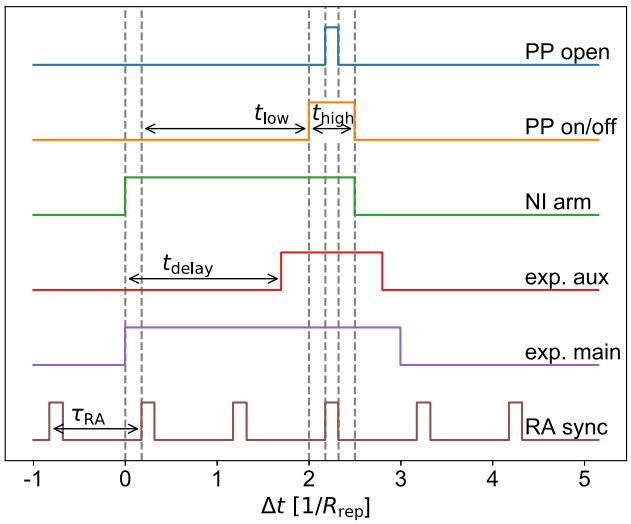

FIG. 2. Diagram describing the timing of each single shot of the experiment. RA sync is a signal indicating that the regenerative amplifier of the laser just fired. Exp. main/aux refers to the exposure of the main and auxiliary camera. NI arm indicates that the pulse generator implemented in the National Instruments card is armed. PP on/off is the output of the pulse generator, which is sent to the pulse picker to enable the input of the laser. PP open is the output window during which the laser opens the pulse picker.

IV. DATA MANAGEMENT AND PRE-PROCESSING

A. Processing *in situ* images

For every individual ablation shot, we record full frame microscopy images on the Andor iXoN 885 camera, before, during, and after the ablation laser pulse, with a 54 × 54 μm^2 field of view. These images are taken *in situ* in the ablation setup. To prevent saturation of the camera, a bandpass filter is used to significantly reduce the intensity of the reflected ablation laser pulse. The filter does not significantly reduce the intensity of the white light used to image the sample surface before and after the ablation has occurred. The before and after images are taken with an exposure time of 200 ms, whereas the exposure time of the during image is 60 μs. This short exposure time ensures that the white light illumination does not significantly contribute to the during image. The image of the sample surface taken before the ablation has occurred can be used to check whether debris was present on the ablation site prior to ablation.

The image of the reflected ablation light can be used to estimate the waist of the laser spot on the sample and measure the reflectivity of the sample under ablation conditions.[25,26] For non-transparent materials such as silicon, the amount of light that is reflected also gives a direct and model independent measure of the amount of light that has been absorbed. Figure 3(a) shows typical images of the reflected ablation spot, organized in the meandering pattern in which they also physically appear on the sample. The sample in this case is a piece of intrinsic $[111] \pm 0.5^\circ$ crystalline silicon wafer. The color scale of these images is left dynamic; in other words, the same gray scale in different sub-images can correspond to different intensities. Furthermore, in this figure and in the subsequent ones, we leave out scale bars and the axis labeling to enable the simultaneous visualization of a large subset of the data. The scale of each sub-image in this figure is 11.2 × 11.2 μm^2.

To determine the waist of the reflected ablation spot, we fit a Gaussian beam profile,

$$I(x,y) = I_0 e^{-2((x-x_0)^2+(y-y_0)^2)/w_0^2},$$

to the image. To determine the total reflected signal, we first subtract the background from the images and subsequently carry out a pixel sum. This background is determined by computing the mean from an image in which the reflected spot is masked out.

The aftermath image offers information on the lateral size of the modified area. Figure 3(b) shows the optical image of the ablation aftermath. These images have been divided by the corresponding *before* images, to compensate for slight inhomogeneities in the illumination.

© Author(s) 2022

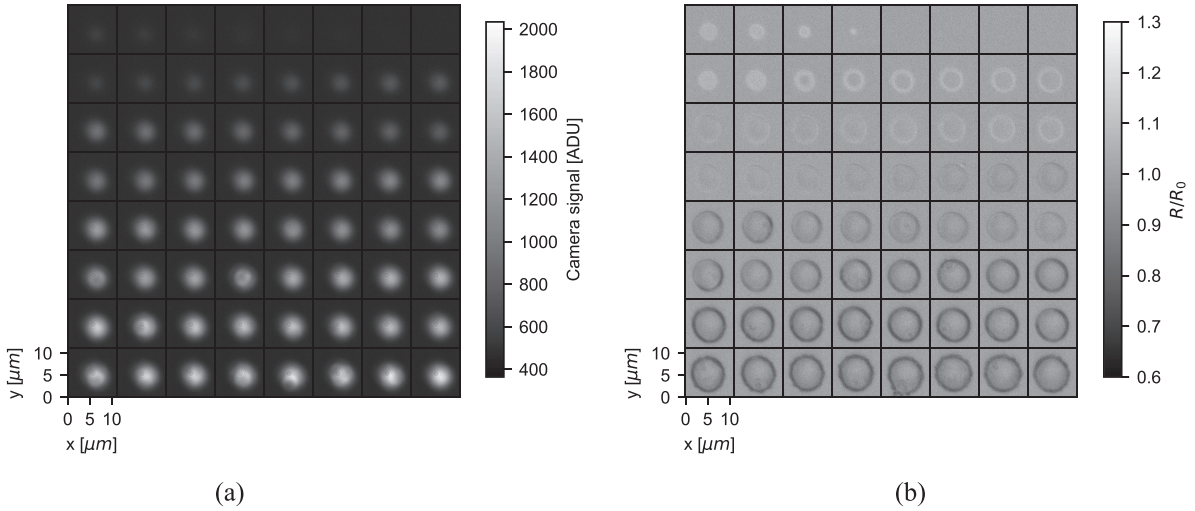

FIG. 3. (a) Camera images of the ablation pulses reflected by the sample, acquired on the main camera. (b) Optical aftermath of the corresponding ablation craters acquired on the main camera. In both (a) and (b), images of 64 individual shots have been arranged in a grid. The scale of each sub-image is 11.2 × 11.2 μm^2.

Analysis of the aftermath images is challenging, mainly for two reasons. First, as can be seen in Fig. 3(b), the central feature in the image qualitatively changes depending on the incident pulse energy. For low fluences, a bright disk is visible in the center. As the fluence is increased, a dark spot appears in the center, which means the central feature has transitioned into a bright ring. For even higher fluences, the most pronounced feature is a dark ring. It should be noted that this behavior may be specific to the material and/or the illumination conditions of the *after* image. Second, the contrast of the images is quite low, making the analysis very sensitive to image noise. We use a combination of numerical filters to smooth the images sufficiently such that we can (with some reliability) automatically locate

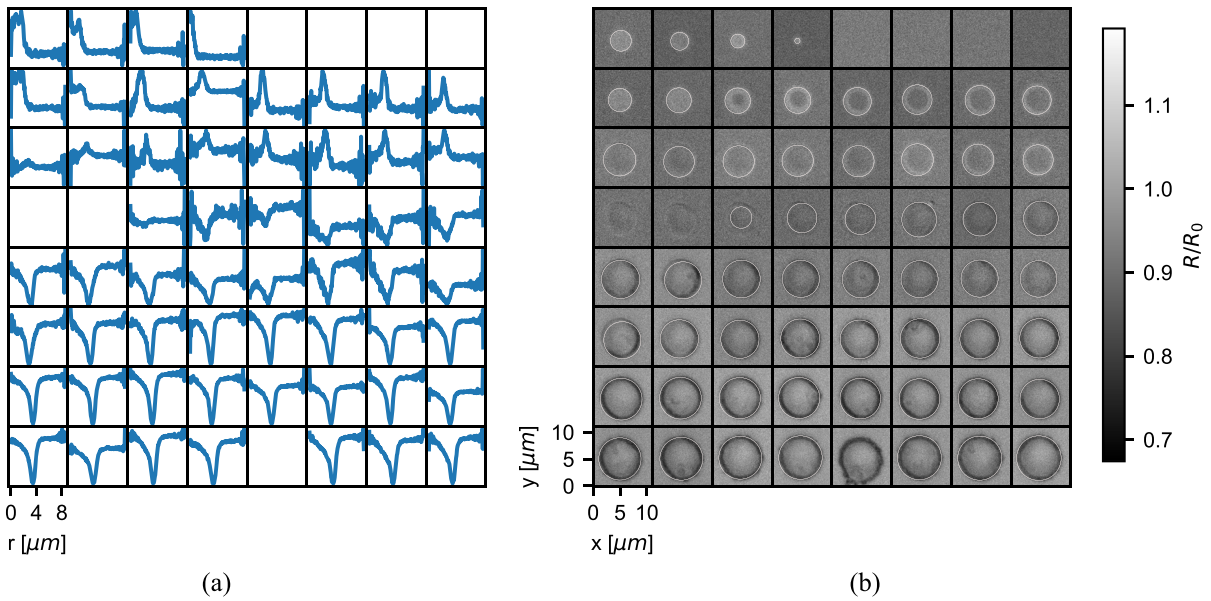

FIG. 4. (a) Radial profiles of the optical aftermath, i.e., the azimuthal average of the images in Fig. 3(b) as a function of the distance to the center of the circular feature. Some subplots are empty, as in these cases, the algorithm failed to identify the center around which to compute the azimuthal average. (b) Optical aftermath of the ablation craters. The circles indicate the outer edge that was found by establishing the outer edge of the peak/dip in the radial profile.

© Author(s) 2022

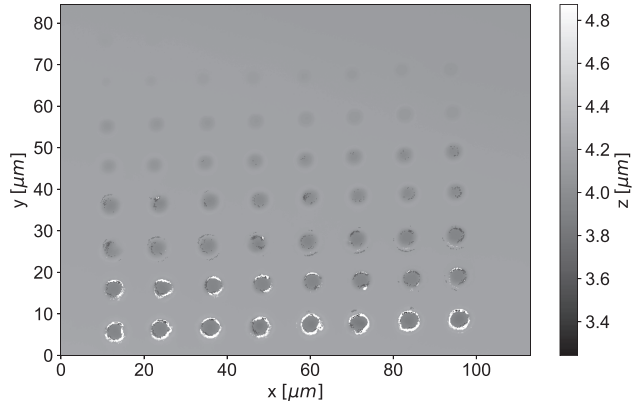

FIG. 5. False-color image, where each pixel represents the height of the silicon surface ablation in run 007 of the experiment. Note that in the raw data, there are invalid data points, which the profilometer stores as 3.4×10^{38} (the largest value that can be stored as a 32 bit float). These invalid points are masked out and appear as white pixels in the image.

the center of the crater. All the details of the analysis can be found in Ref. 27. After this, we compute azimuthal averages around these centers, which results in Fig. 4(a), and fit the peak/dip in the radial profile with a Gaussian function. This allows us to automatically distinguish between the bright and dark rings. We then define the edge by finding the outer radius where the radial profile is halfway between the maximum and the background. The resulting radius is plotted as a red circle in Fig. 4(b). We see that the method, in general, works very well, except in the transition between the bright and dark rings.

B. Processing profilometer data

As mentioned earlier, the depth profile of all craters is measured by using a commercial optical profilometer. The profilometer's field of view is $100 \times 85\ \mu m^2$. The size of the fields generated during the ablation runs was chosen to fit the field of view such that all craters in a single run could be scanned in a single profilometer scan. An example of scan is shown in Fig. 5. The first step in the analysis is to separate the height data into separate arrays for each crater. We do this by manually choosing the position of the lower left crater and the angle that the array has with respect to the x-axis. This angle is caused by a slight rotation of the camera in the profilometer. Each sub-array has a size of 64×64 pixels, which corresponds to $11.2 \times 11.2\ \mu m^2$. The lateral scale of the images is the same as that of the images in Subsection IV A. For craters near the edge of the scan field, the corresponding sub-array is zero padded to reach this size.

The result of the separation is shown in Fig. 6(a). We clearly see that, in the bottom two rows and individual sub-images elsewhere in the figure, the images are effectively black and white. This is due to the fact that there are (patches of) pixels in the images that have a much larger depth than the surrounding pixels. We attribute these to artifacts of the profilometer software algorithm. We remove these artifacts by the following procedure. We first compute the gradient of each image by using the numpy.gradient[28] function. Subsequently, we compute the norm of the gradient. We then identify all pixels for which this norm is larger than 100 nm, meaning that the height makes a sudden step of >100 nm. Finally, we dilate the resulting image and apply the scipy.ndimage.fill_holes[29] algorithm to generate a patch within which we will mask the data. After we have removed these patches, we remove individual hot/cold pixels by removing pixels that are more than ten standard deviations away from the average. As before, for more details, we point to the scripts,

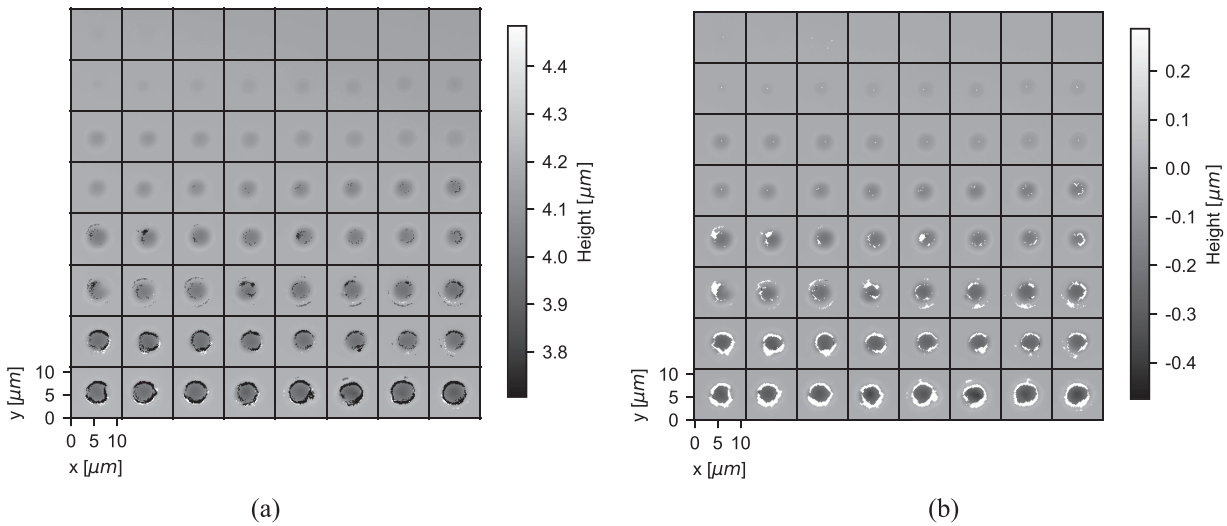

FIG. 6. (a) Separated false-color images, where each pixel represents the height of the silicon surface ablation in run 007 of the experiment. The dimensions of each of the micrographs are $11.2 \times 11.2\ \mu m^2$, thus matching the dimensions of the *in situ* images presented in Figs. 3 and 4(b). (b) Separated false-color images with outliers masked.

© Author(s) 2022

which are available in the data publication. The resulting images are shown in Fig. 6(b).

The next step in the analysis is the leveling of the background, which we achieve by removing the crater from the data using a disk-shaped mask and subsequently fitting a tilted plane to the remaining data. The crater is then unmasked and the tilted plane is subtracted from the data. After this, we estimate the positions of the center of each crater by finding the minimum pixel of a numerically smoothed version of the data. As the last step in the analysis of the image, we fit the generalized Gaussian function,

$$z(x,y) = z_0 + d\, e^{-\left[(|x-x_0|/w)^2+(|y-y_0|/w)^2\right]^{\alpha}},$$

to each image, where z_0 is a residual offset, d is the depth of the crater, (x_0, y_0) is the crater center, and w is the crater width. The exponent α would be 1 for a regular Gaussian function.

In Fig. 7(a), we show cross sections through the craters (blue, solid lines) together with the fit (orange, dashed lines). Note that, although we show cross sections, the fits were carried out on the two-dimensional images. We see that the fits capture the (x,y)-position of the crater excellently but do not fully describe the shape. Therefore, we do not use this fit to determine the ablation depth, but rather the average depth in a small square around the fitted (x,y)-position of the bottom of the crater. The resulting depth is indicated with the gray dashed–dotted lines in Fig. 7(a). Wherever we use the width, we do use the fitted value directly, which means care should be taken when interpreting those results for deep craters.

Finally, to create a convenient overview of all craters in this run, we replot the masked and leveled height data previously shown in Fig. 6(b) on a color scale determined by the crater depth as measured by the procedure described above. Specifically, the white pixels correspond to a height of $0.1 \cdot d$ and black pixels correspond to $-1.1 \cdot d$, with d being the depth of the crater. The resulting images are shown in Fig. 7(b).

C. Data management

All of the Python scripts used to generate the images in this manuscript can be found in the data publication, in the folder RSI_2022_ManuscriptFigures/. These plotting scripts make use of data that have been pre-processed by the Python scripts that can be found in the folder 20210729/PreProcessing. The intermediate results can be verified in pdf files with figures similar to the images presented above, for all (64) ablation runs used in this work. These files can be found in the subfolder 20210729/OverviewFigures/.

The calibration of the auxiliary camera with respect to the thermopile detector (see the Appendix) can be found in the folder 20210915/. The calibration of the thermopile detector with respect to the S314C powermeter can be found in the folder 20210916/.

Data generated during ablation runs on July 29, 2021, are stored in subfolders named 20210729/Data/RawData/run_xyz/, where xyz is the run number. These subfolders contain the images from the auxiliary camera (abc_fluence.npy) and from the main camera (abc_bda.npy) for each shot abc. Furthermore, the folder contains a file xyz_opr.txt, which contains the data from the optical profilometer.

All of the above are stored in a DOI minted vault.

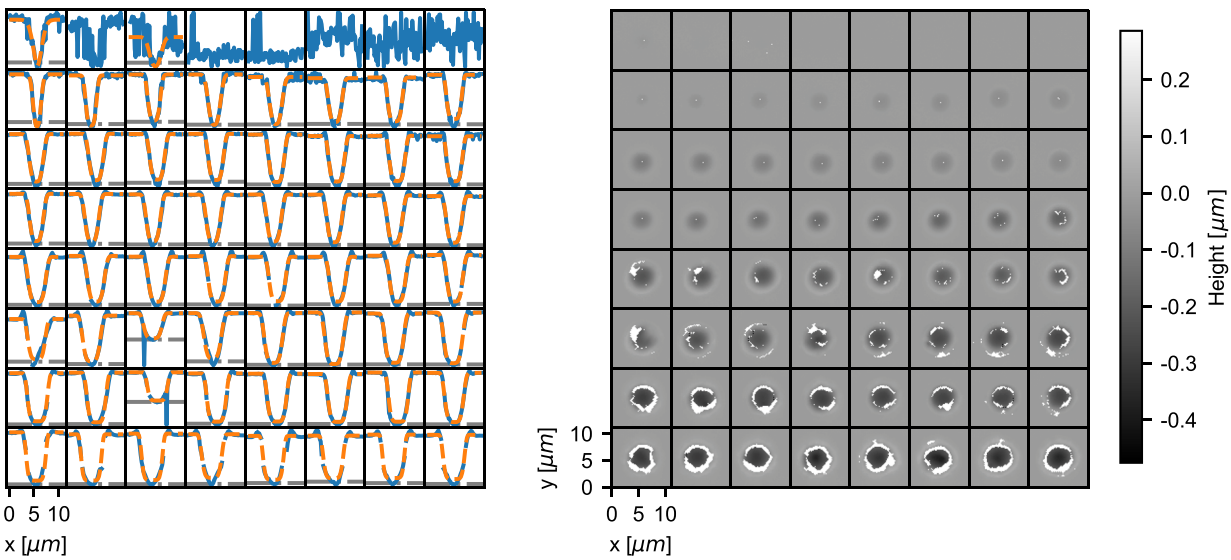

FIG. 7. (a) Cross sections of the height through the bottom of the craters (blue, solid lines), together with a generalized Gaussian fit (orange, dashed lines). The x-dimension of each subplot is 11.2 μm. The scale of the depth for each subplot is adapted to the maximum depth. (b) Separated false-color images; the color scale for each image is set according to the measured depth of the crater.

© Author(s) 2022

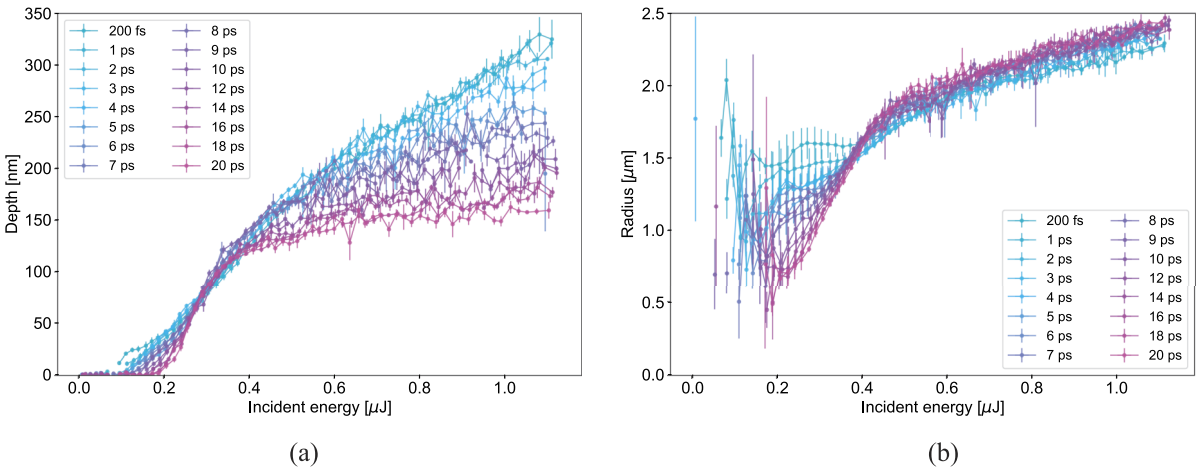

FIG. 8. (a) Ablation depth in nm and (b) crater radius in μm, as determined from the optical profilometry data, as a function of incident pulse energy, for several pulse durations. In both graphs, the error bars indicate the standard deviation over (up to) four craters produced with the same parameters.

V. RESULTS

To demonstrate the strength of our novel apparatus, we now present an analysis of the data preprocessed as described above. As mentioned before, the experiments presented in this work were carried out on a piece of intrinsic crystalline silicon wafer.

Figure 8(a) shows the depth of the craters as a function of incident pulse energies for several pulse durations ranging from 200 fs to 20 ps. In this graph, and the others in this section, each data point is the mean of the result from (up to) four ablated craters with the same setting of the half-wave plate and the error bar is the standard deviation. We see that the depth increases as a function of the incident pulse energy in two stages; until an incident energy of 0.35 μJ, the depth increases rapidly with pulse energy, after which the slope suddenly becomes (much) smaller. The change in slope is subtle for the shortest pulses, but for longer pulses, the effect is much stronger; the initial slope is steeper and the final slope is more moderate than for shorter pulses. It is clear from the graph that for higher pulse energies, the ablation depth is larger for shorter pulses. In Fig. 8(b), we plot the radius of the ablated crater, again obtained by using optical profilometry. We again note a different behavior for short vs long pulses. For long pulses, the radius seems to initially show a slight decrease, followed by a sharp increase, and then a more gentle increase. Short pulses show a large initial radius and a much more gentle initial increase. The final gentle increase in radius (for pulse energies above 0.5 μJ) shows the same slope for all pulse durations used in the experiment, but the shorter pulses

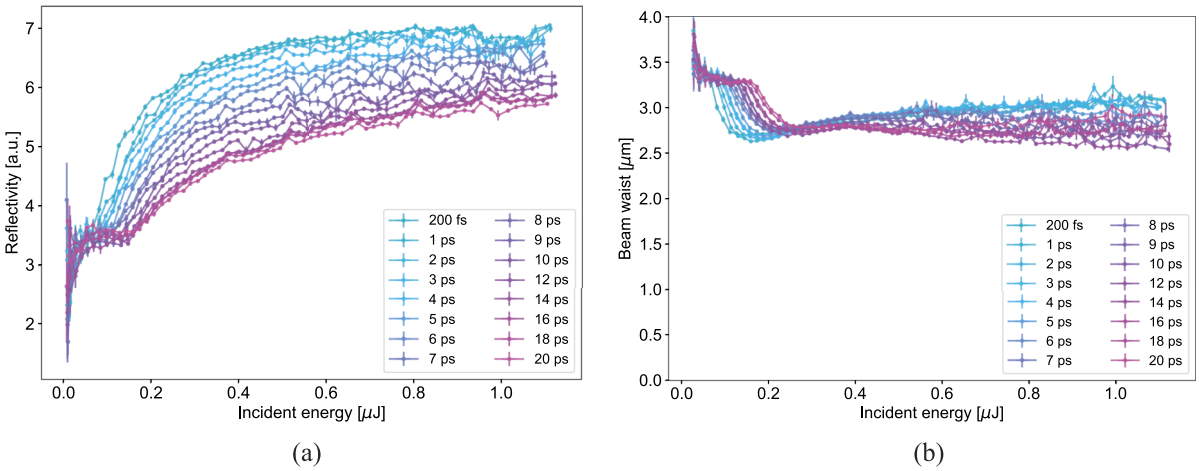

FIG. 9. (a) Self-reflectivity and (b) beam waist of the reflected ablation spot as a function of incident pulse energy for several pulse durations. In both graphs, the error bars indicate the standard deviation over (up to) four shots taken with the same parameters.

© Author(s) 2022

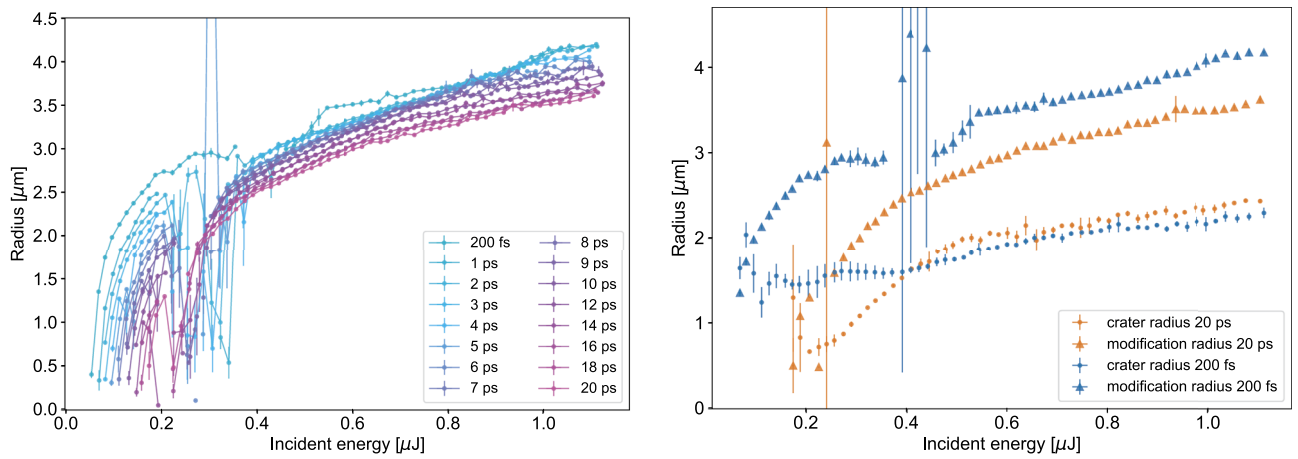

(a) (b)

FIG. 10. (a) Optical modification radius, as determined using *in situ* aftermath imaging, as a function of incident pulse energy, for several pulse durations. (b) Comparison between the normalized topographical crater radius (as determined using optical profilometry, indicated with triangles) and the normalized optical modification radius (as determined using *in situ* imaging, indicated with dots) for 200 fs (blue symbols) and 20 ps (orange symbols) pulse duration. In both graphs, the error bars indicate the standard deviation over (up to) four shots taken with the same parameters.

result in a radius that lies consistently below that of the longer pulses.

In Fig. 9(a), we plot the normalized self-reflectivity, i.e., the reflectivity of the material as it is being excited by the ablation spot, as measured from the images of the reflected ablation spot.[25,26] We note that the self-reflectivity is initially constant, after which it sharply increases for increasing pulse energy. This can be attributed to the generation of a dense electron plasma.[30] If the self-reflectivity increases for higher pulse energy, this effect will be stronger in the center of the ablation spot, where the fluence is highest. This means that the incident Gaussian spot will become slightly more sharply peaked upon reflection, which would lead to a smaller effective beam waist of the reflected ablation spot. In Fig. 9(b), we therefore plot the fitted Gaussian waist of the ablation spot as imaged on the sample

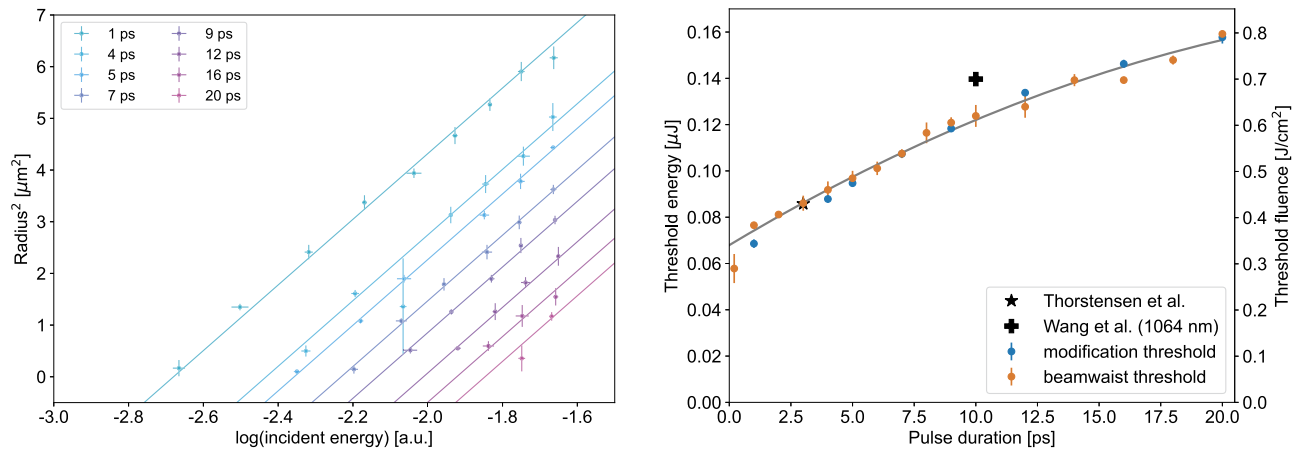

(a) (b)

FIG. 11. (a) Liu plots of the modification radius for several pulse durations. The vertical axis shows the square of the modification radius, and the horizontal axis shows the natural logarithm of the incident energy. The lines represent linear fits, which yield both the incident beam waist and the threshold energy. (b) Threshold obtained from the Liu analysis of the modification radius (blue symbols) and the drop in reflected beam waist (orange symbols) as a function of pulse duration. The gray line is a second-order polynomial simultaneously fitted to both thresholds. For reference, we add experimental values from Thorstensen and Erik Foss[32] and Wang *et al.*[14] The left *y*-axis shows the threshold energy (in μJ), and the right *y*-axis shows the threshold fluence (in J/cm^2).

© Author(s) 2022

surface. We see that for low pulse energies, the fitted waist is roughly constant. For increasing pulse energy, the fitted waist suddenly drops as expected from the above discussion.

Figure 10(a) shows the optical modification radius as measured from the *in situ* optical aftermath, i.e., the radius of the red circles in Fig. 4(b). For low pulse energies, the optical modification radius increases sharply, whereas for larger pulse energies, the optical modification increases more gently at a similar slope for all pulse durations studied. Note that for intermediate pulse energies, the optical modification radius is hard to identify. This is caused by the ring-shaped feature in the aftermath image transitioning from bright to dark. As can be seen by comparison of Figs. 10(a) and 8(b), the optical modification radius is mostly larger than the fitted crater radius. To more easily compare these radii, we combine a subset of the curves in Fig. 10(b). Here, the optical modification radius is indicated with triangles, and the topographical crater radius obtained from optical profilometry is indicated with dots. For clarity, we show only the results for 200 fs (blue symbols) and 20 ps (orange symbols) pulses. We clearly see that the normalized optical modification and topographical crater radii behave very similarly for large incident energies. As *in situ* data are much easier to acquire than optical profilometry data, it is favorable to use the *in situ* modification radius as a measure in experiments where the number of shots taken is so large that acquiring optical profiles for all is unfeasible. As a demonstration, we determine the ablation threshold as a function of pulse duration by using the Liu method.[31] In Fig. 11(a), we show examples of this analysis for various pulse durations. The vertical axis shows the square of the optical modification radius, and the horizontal axis shows the natural logarithm of the pulse energy. The slope of the curve gives the square of the waist of the ablation spot, and the intercept with the horizontal axis yields the threshold. When fitting, the same slope (and thus the same beam waist) is used, whereas the threshold is fitted individually for each pulse duration. We find a beam waist of $w_0 = 3.6 \pm 0.3\ \mu$m. In Fig. 11(b), we plot (in blue) the resulting threshold as a function of pulse duration. The left y-axis shows the threshold energy, whereas the right y-axis shows the threshold fluence. To make the conversion between pulse energy and pulse fluence, we used the beam waist determined above.

Alternatively, we can identify the pulse energy at which the sharp drop in fitted waist of the reflected ablation spot occurs, as can be seen in Fig. 9(b). It is reasonable to assume that this drop occurs at the point of dielectric breakdown, which is known to correlate with the ablation threshold.[33] The threshold associated with this drop is also plotted in Fig. 11(b) and we, indeed, see an excellent agreement between both methods of obtaining the threshold. The gray line is a second-order polynomial simultaneously fitted to both thresholds, used as a guide to the eye. Also presented in this plot are values obtained from the literature, specifically those by Thorstensen and Erik Foss[32] and Wang *et al.*,[14] where it should be noted that the latter is the threshold at a center wavelength of 1064 nm (as opposed to ~1030 nm used by Thorstensen and Erik Foss and in our work).

Finally, to verify that the ablation threshold obtained from these *in situ* measurements agrees with the result from the optical profiles, we re-plot the depth as previously shown in Fig. 8(a), with the incident energy scaled to the threshold energy for each pulse duration. As we can clearly see in Fig. 12, the ablation depth, indeed, drops to zero at a normalized incident energy of 1. This is a non-trivial result, as the ablation threshold was obtained without making use of the depth data. This further proves that using *in situ* data in ablation studies can offer quantitative results.

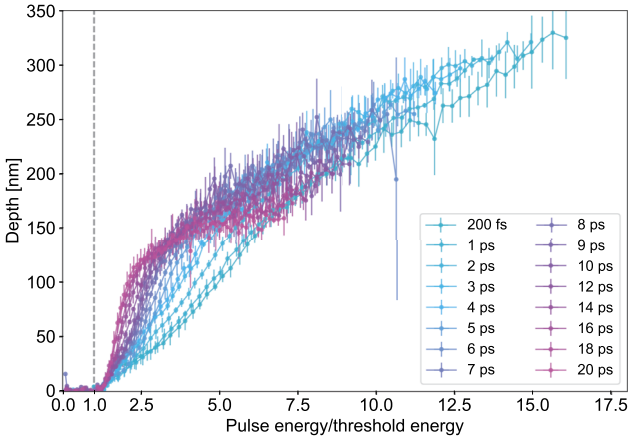

FIG. 12. Ablation depth (in nm) plotted as a function of the pulse energy normalized to the threshold energy. Note that for all pulse durations, the depth, indeed, drops to zero with the normalized pulse energy approaches unity.

VI. CONCLUSION

In summary, we presented a novel experimental apparatus that enables rapid and systematic ablation studies. The highly automated operation of the setup allows the exploration of large parameter space, for instance, systematically moving from single pulse, double pulse, and even pulse train experiments. A smaller, portable version of the apparatus is also under development. This version can conveniently be transported to facilities with other light sources.

We have shown that *in situ* images of the sample surface after the ablation and *in situ* images of the reflected ablation spot both yield measures that can be used to draw quantitative conclusions about the ablation threshold. This is crucial for large, systematic studies, as it means that time-consuming and potentially expensive characterization measurements, such as optical profilometry, scanning electron microscopy, and atomic force microscopy, do not have to be routinely obtained for all craters.

To demonstrate the apparatus, we have used the (publicly available) dataset presented in this paper to determine the pulse duration dependence of the ablation threshold in crystalline silicon.

ACKNOWLEDGMENTS

This publication is part of the project "Wafer damage control: understanding and preventing light-induced material changes in optical measurement systems" (with Project No. 17963) of the research program High Tech Systems and Materials (HTSM), which is (partly) financed by the Dutch Research Council (NWO). The project is co-financed by ASM Laser Separation International (ALSI)

© Author(s) 2022

and ASML. The authors thank Paul Planken, Javier Hernandez Rueda, and Vina Faramarzi for the careful reading of the manuscript and Paul Jurrius, Dante Killian, Aron Opheij, Cees de Kok, Guido de Haan, Ester Abram, Dimitry Lamers, and Igor Hoogsteder for technical support.

AUTHOR DECLARATIONS

Conflict of Interest

The authors have no conflicts to disclose.

Author Contributions

Marnix Vreugdenhil: Conceptualization (equal); Data curation (equal); Formal analysis (equal); Investigation (equal); Methodology (equal); Project administration (equal); Software (equal); Validation (equal); Visualization (equal); Writing – original draft (equal); Writing – review & editing (equal). **Dries van Oosten:** Conceptualization (equal); Data curation (equal); Formal analysis (equal); Funding acquisition (equal); Investigation (equal); Methodology (equal); Project administration (equal); Resources (equal); Software (equal); Supervision (equal); Validation (equal); Visualization (equal); Writing – original draft (equal); Writing – review & editing (equal).

DATA AVAILABILITY

The data that support the findings of this study are openly available on Utrecht University DOI-minted data repository YODA at https://doi.org/10.24416/UU01-0XSGWO, https://doi.org/10.24416/UU01-X3HYK2, and https://doi.org/10.24416/UU01-DWN2HT. The scripts that produce the figures can be found at https://doi.org/10.24416/UU01-QNG5Y4.

APPENDIX: PULSE ENERGY CALIBRATION

To determine the pulse energy on a single-shot basis, we calibrate the signal on the auxiliary camera with respect to a power meter placed underneath the microscope objective. During calibration, we run the laser at a relatively low repetition rate of 500 Hz (by setting the pulse picker division ratio at 100), in order to keep the average intensity on optical components low enough to prevent thermal damage. This low repetition rate has the downside that it makes use of a sensitive photodiode-based power meter unpractical, yet the low average power (on the order of a few hundred microwatt) underneath the objective is challenging to measure using a commercial thermal power head. We therefore employ the following strategy. We mount a thermopile sensor (Thorlabs TD10XP) on a sample holder that reproducibly fits in the ablation setup on the position where the sample is mounted during experiments (see Fig. 1 of the main text). The thermopile signal is amplified by using a Stanford Research preamplifier (SR650) set to an amplification of 1000 × and with the input filter configured as a 3 Hz, 12 dB/oct. low-pass filter. The output from the SR650 is connected to an analog input on a National Instrument USB-6211. The analog input is configured as a differential input, with the other input connected to an analog output; this arrangement allows us to zero the amplified thermopile signal.

As the TD10XP is supplied without a calibration certificate, we have to measure the sensitivity of the sensor by ourselves. We do this by measuring the power directly after the polarizing beam splitter with the arrangement discussed above and with a Thorlabs S314C thermal head connected to a Thorlabs PM100D readout unit. With the Thorlabs power meter, we measure a power of 79 ± 0.5 mW. The amplified signal from the TD10XP as measurement by the national instruments card is 7.98 ± 0.08 V. Dividing these numbers, we find a sensitivity of $S = (101 \pm 1)$ mV/mW, which agrees well with the typical sensitivity of 100 mV/W stated by the supplier (in combination with the 1000× amplification).

It is important to note that the average power we measured here does not correspond to 1/100th of the laser power, as one might naively expect. This is because the pulse picker does not fully block light when it is closed, and at high pulse picker division ratios, this leakage can lead to a substantial contribution. Specifically, the average power will behave like

$$P_{\mathrm{avg}}(\alpha) = \left(1 - \frac{1}{\alpha}\right)P_{\mathrm{leak}} + \frac{1}{\alpha}P_{\mathrm{avg}}(1),$$

where α is the pulse picker divider ratio, and P_{leak} is the power that is transmitted through the closed pulse picker. To determine P_{leak}, we measure the laser power (with the S314C thermal head) for division ratios of 1, 10, 20, . . ., 100 and fit to the above function. We find that $P_{\mathrm{leak}} = 16.8 \pm 0.14$ mW. The fraction of energy in the picked pulses is therefore $F = (P_{\mathrm{avg}} - P_{\mathrm{leak}})/P_{\mathrm{avg}} = 0.787 \pm 0.002$.

The final step in calibrating the auxiliary camera is to simultaneously acquire a camera signal and the amplified thermopile signal. For a given angle of the $\lambda/2$ plate, we first take 50 images with the beam shutter closed, then 125 images with the beam shutter opened, followed by 125 images with the beam shutter closed. The location of the waveplate and the beam shutter can be found in Fig. 1 of the main text. We take these calibration data at a rate of ~20 fps, which means we do not capture all laser pulses. The exposure time of the camera is chosen such that we capture exactly one laser pulse per frame and avoid signal from leakage in the pulse picker.

To process the camera images, we sum over the image after subtracting a background level. We subsequently compute the mean and standard deviation of the images taken with the beam shutter open and those taken with the beam shutter closed. Although subtracting these numbers, we arrive at the mean number N of camera counts per pulse.

To process the thermopile signal, we compute the mean of the first 50 data points, which should contain only a small offset. We subtract this mean from 125 data points taken with the shutter open. To account for the rise time of the sensor, we fit to the following function:

$$V(t) = V_0\left(1 - e^{-t/\tau}\right).$$

Both the number of camera counts per pulse and V_0 follow a sinusoidal pattern as a function of the angle ϕ of the wave plate,

© Author(s) 2022

$$f(\phi) = f_{\max}\,\sin(\phi - \phi_0).$$

By fitting $N(\phi)$ and $V_0(\phi)$ to the above function and averaging the results of several calibration runs, we find $N_{\max} = 6.60 \cdot 10^5 \pm 3 \cdot 10^3$, $V_{0,\max} = (52.3 \pm 0.9)$ mV, and $\phi_0 = (6.13 \pm 0.08)^\circ$. This leads to a conversion factor of $A = 7.9 \cdot 10^{-5} \pm 1 \cdot 10^{-6}$ μV/count. The final calibration factor then becomes

$$C = \frac{FA}{SR},$$

with R being the repetition frequency. Evaluating this expression and propagating the uncertainties leads to $C = 1.24 \pm 0.03$ pJ/count.

REFERENCES

[1] A. Yokotani, T. Mukumoto, T. Mizuno, K. Kurosawa, K. Kawahara, T. Ninomiya, and H. Sawada, "Development of dicing technique for thin semiconductor substrates with femtosecond laser ablation," Proc. SPIE **5339**, 374–381 (2004).

[2] H. K. Toenshoff, A. Ostendorf, K. Koerber, and N. Baersch, "Speed-rate improvement for microcutting of thin silicon with femtosecond laser pulses," Proc. SPIE **4830**, 531–536 (2003).

[3] K. Sugioka and Y. Cheng, "Femtosecond laser three-dimensional micro- and nanofabrication," Appl. Phys. Rev. **1**, 041303 (2014).

[4] N. Ahmed, S. Darwish, and A. M. Alahmari, "Laser ablation and laser-hybrid ablation processes: A review," Mater. Manuf. Processes **31**, 1121–1142 (2016).

[5] K. C. Phillips, H. H. Gandhi, E. Mazur, and S. K. Sundaram, "Ultrafast laser processing of materials: A review," Adv. Opt. Photonics **7**, 684–712 (2015).

[6] B. N. Chichkov, C. Momma, S. Nolte, F. von Alvensleben, and A. Tünnermann, "Femtosecond, picosecond and nanosecond laser ablation of solids," Appl. Phys. A **63**, 109–115 (1996).

[7] S. K. Sundaram and E. Mazur, "Inducing and probing non-thermal transitions in semiconductors using femtosecond laser pulses," Nat. Mater. **1**, 217–224 (2002).

[8] T. Y. Choi and C. P. Grigoropoulos, "Observation of femtosecond laser-induced ablation in crystalline silicon," J. Heat Transfer **126**, 723–726 (2004).

[9] B. Rethfeld, D. S. Ivanov, M. E. Garcia, and S. I. Anisimov, "Modelling ultrafast laser ablation," J. Phys. D: Appl. Phys. **50**, 193001 (2017).

[10] J. Zhang, M. Gecevičius, M. Beresna, and P. G. Kazansky, "Seemingly unlimited lifetime data storage in nanostructured glass," Phys. Rev. Lett. **112**, 033901 (2014).

[11] H. Wang, Y. Lei, L. Wang, M. Sakakura, Y. Yu, G. Shayeganrad, and P. G. Kazansky, "100-layer error-free 5D optical data storage by ultrafast laser nanostructuring in glass," Laser Photonics Rev. **16**, 2100563 (2022).

[12] G. Bonamis, E. Audouard, C. Hönninger, J. Lopez, K. Mishchik, E. Mottay, and I. Manek-Hönninger, "Systematic study of laser ablation with GHz bursts of femtosecond pulses," Opt. Express **28**, 27702–27714 (2020).

[13] P. P. Pronko, P. A. VanRompay, C. Horvath, F. Loesel, T. Juhasz, X. Liu, and G. Mourou, "Avalanche ionization and dielectric breakdown in silicon with ultrafast laser pulses," Phys. Rev. B **58**, 2387–2390 (1998).

[14] X. Wang, Z. H. Shen, J. Lu, and X. W. Ni, "Laser-induced damage threshold of silicon in millisecond, nanosecond, and picosecond regimes," J. Appl. Phys. **108**, 033103 (2010).

[15] P. Allenspacher, B. Huettner, and W. Riede, "Ultrashort pulse damage of Si and Ge semiconductors," Proc. SPIE **4932**, 358–365 (2003).

[16] J. Bonse, S. Baudach, J. Krüger, W. Kautek, and M. Lenzner, "Femtosecond laser ablation of silicon–modification thresholds and morphology," Appl. Phys. A **74**, 19–25 (2002).

[17] B. C. Stuart, M. D. Feit, S. Herman, A. M. Rubenchik, B. W. Shore, and M. D. Perry, "Nanosecond-to-femtosecond laser-induced breakdown in dielectrics," Phys. Rev. B **53**, 1749–1761 (1996).

[18] L. A. Emmert, M. Mero, and W. Rudolph, "Modeling the effect of native and laser-induced states on the dielectric breakdown of wide band gap optical materials by multiple subpicosecond laser pulses," J. Appl. Phys. **108**, 043523 (2010).

[19] R. Stoian, D. Ashkenasi, A. Rosenfeld, and E. E. B. Campbell, "Coulomb explosion in ultrashort pulsed laser ablation of Al_2O_3," Phys. Rev. B **62**, 13167–13173 (2000).

[20] C. W. Carr, H. B. Radousky, and S. G. Demos, "Wavelength dependence of laser-induced damage: Determining the damage initiation mechanisms," Phys. Rev. Lett. **91**, 127402 (2003).

[21] L. Gallais, D.-B. Douti, M. Commandré, G. Batavičiūtė, E. Pupka, M. Ščiuka, L. Smalakys, V. Sirutkaitis, and A. Melninkaitis, "Wavelength dependence of femtosecond laser-induced damage threshold of optical materials," J. Appl. Phys. **117**, 223103 (2015).

[22] J. Hernandez-Rueda, J. Clarijs, D. van Oosten, and D. M. Krol, "The influence of femtosecond laser wavelength on waveguide fabrication inside fused silica," Appl. Phys. Lett. **110**, 161109 (2017).

[23] K. Venkatakrishnan, B. Tan, P. Stanley, and N. R. Sivakumar, "The effect of polarization on ultrashort pulsed laser ablation of thin metal films," J. Appl. Phys. **92**, 1604–1607 (2002).

[24] J. M. Binder, A. Stark, N. Tomek, J. Scheuer, F. Frank, K. D. Jahnke, C. Müller, S. Schmitt, M. H. Metsch, T. Unden, T. Gehring, A. Huck, U. L. Andersen, L. J. Rogers, and F. Jelezko, "Qudi: A modular python suite for experiment control and data processing," SoftwareX **6**, 85–90 (2017).

[25] H. Zhang, D. M. Krol, J. I. Dijkhuis, and D. van Oosten, "Self-scattering effects in femtosecond laser nanoablation," Opt. Lett. **38**, 5032–5035 (2013).

[26] J. Hernandez-Rueda and D. van Oosten, "Transient scattering effects and electron plasma dynamics during ultrafast laser ablation of water," Opt. Lett. **44**, 1856–1859 (2019).

[27] M. Vreugdenhil and D. van Oosten, "A highly automated apparatus for ultrafast laser ablation studies: Figures and analysis code," Data Publication Platform of Utrecht University (2022).

[28] NumPy, numpy.gradient, https://numpy.org/doc/stable/reference/generated/numpy.gradient.html, 2022 (last accessed 31 January 2022).

[29] SciPy, scipy.ndimage.binary_fill_holes, https://docs.scipy.org/doc/scipy/reference/generated/scipy.ndimage.binary_fill_holes.html, 2022 (last accessed 31 January 2022).

[30] H. Zhang, S. A. Wolbers, D. M. Krol, J. I. Dijkhuis, and D. van Oosten, "Modeling and experiments of self-reflectivity under femtosecond ablation conditions," J. Opt. Soc. Am. B **32**, 606–616 (2015).

[31] J. M. Liu, "Simple technique for measurements of pulsed Gaussian-beam spot sizes," Opt. Lett. **7**, 196–198 (1982).

[32] J. Thorstensen and S. Erik Foss, "Temperature dependent ablation threshold in silicon using ultrashort laser pulses," J. Appl. Phys. **112**, 103514 (2012).

[33] I. Mirza, N. M. Bulgakova, J. Tomáštík, V. Michálek, O. Haderka, L. Fekete, and T. Mocek, "Ultrashort pulse laser ablation of dielectrics: Thresholds, mechanisms, role of breakdown," Sci. Rep. **6**, 39133 (2016).

© Author(s) 2022